

Article

Distribution and Driving Mechanism of N₂O in Sea Ice and Its Underlying Seawater during Arctic Melt Season

Jian Liu ^{1,2}, Liyang Zhan ^{2,*}, Qingkai Wang ³, Man Wu ², Wangwang Ye ², Jiexia Zhang ², Yuhong Li ², Jianwen Wen ² and Liqi Chen ^{1,2,*}

¹ College of Ocean and Earth Sciences, Xiamen University, Xiamen 361000, China; liujian@tio.org.cn

² Key Laboratory of Global Change and Marine-Atmospheric Chemistry, Third Institute of Oceanography, Ministry of Natural Resources, Xiamen 361000, China; wuman@tio.org.cn (M.W.); yewangwang@tio.org.cn (W.Y.); zhangjiexia@tio.org.cn (J.Z.); liyuhong@tio.org.cn (Y.L.); wenjianwen@tio.org.cn (J.W.)

³ State Key Laboratory of Coastal and Offshore Engineering, Dalian University of Technology, Dalian 116024, China; wangqingkai@dlut.edu.cn

* Correspondence: zhanliyang@tio.org.cn (L.Z.); chenliqi@tio.org.cn (L.C.)

Abstract: Nitrous oxide (N₂O) is the third most important greenhouse gas in the atmosphere, and the ocean is an important source of N₂O. As the Arctic Ocean is strongly affected by global warming, rapid ice melting can have a significant impact on the N₂O pattern in the Arctic environment. To better understand this impact, N₂O concentration in ice core and underlying seawater (USW) was measured during the seventh Chinese National Arctic Research Expedition (CHINARE2016). The results showed that the average N₂O concentration in first-year ice (FYI) was 4.5 ± 1.0 nmol kg⁻¹, and that in multi-year ice (MYI) was 4.8 ± 1.9 nmol kg⁻¹. Under the influence of exchange among atmosphere-sea ice-seawater systems, brine dynamics and possible N₂O generation processes at the bottom of sea ice, the FYI showed higher N₂O concentrations at the bottom and surface, while lower N₂O concentrations were seen inside sea ice. Due to the melting of sea ice and biogeochemical processes, USW presented as the sink of N₂O, and the saturation varied from 47.2% to 102.2%. However, the observed N₂O concentrations in USW were higher than that of T-N₂O_{USW} due to the sea-air exchange, diffusion process, possible N₂O generation mechanism, and the influence of precipitation, and a more detailed mechanism is needed to understand this process in the Arctic Ocean.

Keywords: nitrous oxide; Arctic Ocean; sea ice; underlying seawater; ice melting



Citation: Liu, J.; Zhan, L.; Wang, Q.; Wu, M.; Ye, W.; Zhang, J.; Li, Y.; Wen, J.; Chen, L. Distribution and Driving Mechanism of N₂O in Sea Ice and Its Underlying Seawater during Arctic Melt Season. *Water* **2022**, *14*, 145. <https://doi.org/10.3390/w14020145>

Academic Editor: Bruno Charrière

Received: 15 September 2021

Accepted: 4 January 2022

Published: 7 January 2022

Publisher's Note: MDPI stays neutral with regard to jurisdictional claims in published maps and institutional affiliations.



Copyright: © 2022 by the authors. Licensee MDPI, Basel, Switzerland. This article is an open access article distributed under the terms and conditions of the Creative Commons Attribution (CC BY) license (<https://creativecommons.org/licenses/by/4.0/>).

1. Introduction

N₂O is the third most important greenhouse gas in the atmosphere and the fastest growing ozone-destroying gas in terms of emissions, and its global warming potential (GWP) is 310 times that of equal-molecular CO₂. The N₂O mixing ratio in the atmosphere has reached 332 nL L⁻¹ [1]. Oceans are an important natural source of N₂O, accounting for about 20% of the global N₂O sources [2]. It is generally thought that marine N₂O is mainly generated by microbial ammonia oxidation, denitrification, and nitrifier-denitrification process, whereas denitrification in an oxygen-depleting environment is the main sink of N₂O. The Arctic Ocean is one of the regions most impacted by climate change. Under the influence of atmospheric circulation, Arctic Oscillation and inputs of warm waters from the Pacific Ocean, the Arctic sea ice has a rapidly modifying structure, thickness, coverage, and chemical composition [3], with possible feedback effects on Arctic ecosystems [4,5]. Previous studies in the Arctic Ocean have mainly focused on the distribution and partial metabolic process of N₂O in the open ocean. These studies described the N₂O distribution of surface [6], the anomalous high value of N₂O in the subsurface [7], and widespread N₂O production and consumption processes in the Arctic Ocean [8]. The Arctic Ocean has a long winter, and about 1.52×10^7 km² of the ocean is covered by sea ice [9]. Previously, Arctic

sea ice was considered airtight and an isolation barrier for sea–air exchange. However, more recent studies have shown that there is gas exchange among the atmosphere–sea ice–seawater system [10]; as a consequence, sea ice can also act as an important source and sink of atmospheric biogenic gases [11,12].

Hitherto, there are few studies on N₂O in sea ice and underlying seawater (USW), and only two studies on N₂O distribution in Arctic sea ice. Randall et al. [13] investigated the distribution of N₂O in the bottom 10 cm of sea ice and USW for the first time, and confirmed that N₂O in sea ice is transported to the ocean during autumn and winter. In addition, N₂O is ventilated into the atmosphere and sea ice appears as a seasonal source of this gas. Nevertheless, the melting of sea ice in spring and summer makes surface seawater undersaturated with N₂O, presenting a seasonal N₂O sink [14,15]. However, there is still no research on the dilution process of N₂O in USW caused by the melting of sea ice. The study presented herein investigated the profile distribution mechanism of N₂O in first-year ice (FYI), multi-year ice (MYI) and USW, and combined that profile with a salinity gradient analysis to determine the effect of melting Arctic Sea ice on N₂O concentration in USW.

2. Materials and Methods

2.1. Study Area

The Arctic Ocean is the smallest ocean in the world, has the highest salinity, and has an average depth of 1200 m. It is covered by sea ice most of the year except during summer. There is a polar high in the Arctic, and its southward movement tends to affect temperatures over much of the northern hemisphere. Melt ice water, shelf runoff, Pacific inflow water, and Atlantic water together constitute the main body of the upper middle layer of water in the Western Pacific, and the surface water is mainly the mixed water formed after the melting of sea ice [16]. The Arctic Oscillation (AO) is the main characteristic of the arctic atmospheric circulation, and the AO index is generally used to represent the strength of the AO [17]. When AO is in a positive phase, the strength of the polar vortex is small, which is conducive to the maintenance of polar westerlies and the weakening of poleward transport. When the AO is in a negative phase, the Arctic Ocean is controlled by high pressure, making it easier for cold air to move south. Influenced by the Arctic Oscillation, the Beaufort vortex exists for a long time, and the transpolar current carries a large amount of sea ice and Pacific water across the pole into the Greenland Sea, thus affecting the global thermohaline circulation process. The Arctic Ocean Oscillation (AOO) is used to assess the characteristics of the arctic wind-driven circulation [18]. When AOO is negative, the cyclones force the sea ice to drift counterclockwise. When AOO is positive, the anticyclones force sea ice to drift clockwise [18,19]. Sea ice in the Arctic has been declining at an alarming rate in recent years due to the rapid warming of the Arctic caused by abrupt changes in the region's atmosphere, ice, and ocean systems [20–22]. Satellite observations show that the extent of arctic summer sea ice has been declining by more than 10 percent every decade [23], reaching 341,000 km² in September 2021, the lowest since observations began. Current models estimate that the Arctic Ocean will be free of summer sea ice for the first time in 2054–2058 [24].

Seawater and sea ice samples were collected during the seventh Chinese National Arctic Research Expedition (CHINARE2016) in the Arctic in September 2016. As shown in Figure 1, three ice stations were sampled, named as SI05, SI06, and Long Ice. Ice stations were selected according to the floating ice conditions during the voyage. All stations were located on vast ice floes with an area of several square kilometers; among these, SI06 (76°18.63' N, 179°35.76' E) was located in the Chukchi Sea, and Long Ice (82°52.81' N, 159°42.42' W) and SI05 (79°56.23' N, 179°23.02' W) were located in the central Arctic Ocean. Long Ice is a long-term ice station, and SI05 and SI06 are short-term ice stations. All samples were taken in August 2016, when the sea ice was melting rapidly. Sea ice and seawater samples were collected at SI05 and SI06 stations, while multiple ice water data were mainly collected at Long Ice station. The sampling sites were located in the flat interior of the floating ice, away from the ice edge and melt ponds.

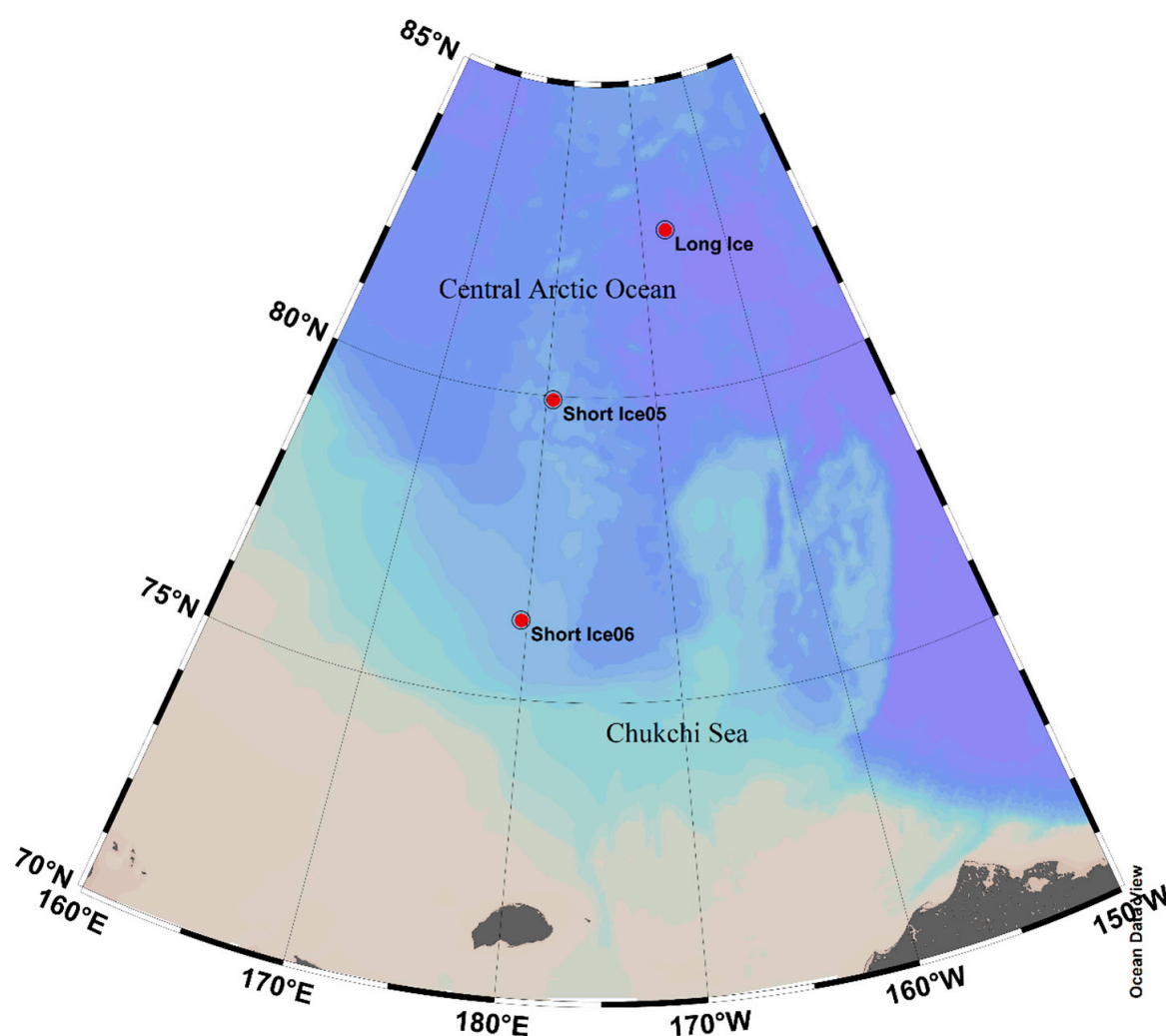


Figure 1. Map of ice stations during CHINARE 2016. The sampling times were 18 August 2016 (SI05), 20 August 2016 (SI06) and 14 August 2016 (Long Ice), respectively.

2.2. Sampling and Processing

The ice core samples were drilled using a drilling auger 9 cm in diameter, and at least 3 ice cores were taken for each sampling site. In total, ice core profiles were collected at two stations (IS05 and IS06), and five USW profiles were collected at three stations (IS05, IS06 and Long Ice). The total sampling time for each ice station operation is less than 30 min. The distances between ice cores were less than 1 m to limit spatial variability and the temperature, salinity, density and N_2O concentration of ice cores were measured respectively. The USW was pumped using an electric peristaltic pump through silicone tube from ice holes formed by collecting ice cores, at the depths of 0, 0.6, 1.1, and 1.6 m beneath the bottom ice, respectively. After the thermohaline parameters were measured on-site with a WTW Cond 3110 probe, the silicone tube was inserted into the bottom of a 250 mL frosted-glass bottle, and filled to overflowing with three times the sample volume. Afterwards, the sample was poisoned with 150 μ L of saturated $HgCl_2$ solution and sealed with ground glass stopper and vacuum grease for storage. The N_2O concentration was measured in the laboratory. The ice core was cut into columns with a length of \sim 20 cm and placed in Polyvinyl Fluoride (PVF) airtight bags for sealing. Additionally, airtight bags were vacuumized and melted in a cold room (\sim 4 $^{\circ}C$). After the sea ice melted, it was sealed and stored in the same way as previous treatment of seawater and brought back to the laboratory for analysis.

The sea ice temperature was measured at each site immediately after lifting the ice core using a fast-response probe thermometer (accuracy ± 0.2 °C, Testo, Germany). The probe was inserted in 2 mm diameter holes drilled to the core center at 5 to 10 cm intervals along the core length [25]. In order to avoid the loss of brine in the ice cores, the ice cores were treated quickly in the field to reduce the salinity error [26,27]. The density of the ice core was taken back to the land laboratory for measurement via a method based on Wang et al. [25]. The temperature, salinity, and density of the ice core were provided by the Dalian University of Technology.

2.3. Laboratory Analysis

After the samples were brought back to the laboratory, the seawater samples were divided into 20 mL headspace bottles, and nitrogen gas was used for headspace. After headspace, the gas volume was about 9 mL, while the water sample volume was about 11 mL. After equilibrium was achieved, the 1 mL gas sample was injected into gas chromatography with an electron capture detector (ECD) by an automatic sampler for analysis [28]. N₂O concentration was calculated according to previous research methods [29]. The coefficient of variation of serial gas-certified reference materials for nitrous oxide in nitrogen (GBW08151) provided by the National Center for Standard Substances was 2%, and the coefficient of variation of this method for determining N₂O concentration was also 2% [28].

2.4. Computational Method

The N₂O saturation and saturation anomaly (SA) was calculated as follows:

$$\text{Saturation} = \frac{C_{\text{ob}}}{C_{\text{eq}}} \times 100\% \quad (1)$$

$$\text{SA} = \frac{\Delta C}{C_{\text{eq}}} = \frac{C_{\text{ob}} - C_{\text{eq}}}{C_{\text{eq}}} \times 100\% \quad (2)$$

where C_{ob} is the measured N₂O concentration in seawater, C_{eq} is the equilibrium concentration; the Brine salinity and volume fraction (brine volume account for percentage of sea ice volume) in sea ice was calculated as follows ($T > -2$ °C) [30]:

$$\text{BrV} = \left(1 - \frac{V_a}{V}\right) \times \frac{\rho_i S}{(S_b - S)\rho_b + \rho_i S} \quad (3)$$

where V_a represents gas volume, V represents total sea ice volume, ρ_i represents pure water ice density, ρ_b represents brine density, S represents sea ice salinity, and S_b represents brine salinity. Additionally, ρ_i , S_b , ρ_b are calculated as follows:

$$\rho_i \left(\frac{\text{g}}{\text{cm}^3}\right) = 0.917 - 1.043 \times 10^{-4}T \quad (4)$$

$$S_b = \frac{T}{T - T_1} \times 1000 \quad (5)$$

$$\rho_b = 1 + 0.0008 \times S_b \quad (6)$$

where T_1 is a constant and the value is 54.11 °C.

In order to study the distribution mechanism of N₂O in sea ice, we assumed that the N₂O in gaseous phase of sea ice was ventilated to the atmosphere and brine was in equilibrium with atmosphere N₂O partial pressure based on the permeability of sea ice. Then we could calculate the presumed N₂O concentration ($T\text{-N}_2\text{O}_{\text{ice}}$) according to sea ice brine and gas volume fractions:

$$\text{N}_2\text{O}_{\text{ice}} = \text{N}_2\text{O}_{\text{br}} + \text{N}_2\text{O}_{\text{g}} \quad (7)$$

where N_2O_{br} (nmol kg^{-1}) represents the amount of N_2O in brine in 1 kg of sea ice, the amount of brine is calculated by Formula (3), and the N_2O concentration in brine was calculated according to Weiss and Price [29]; N_2O_g (nmol kg^{-1}) represents the amount of N_2O in gas in 1 kg of sea ice. In addition, the theoretical N_2O concentration ($T\text{-}N_2O_{USW}$) of mixed USW could be calculated as follows:

$$X_{ICE} + X_{WRW} = 1 \quad (8)$$

$$S_{ICE} \times X_{ICE} + S_{WRW} \times X_{WRW} = 1 \quad (9)$$

$$T\text{-}N_2O_{USW} = N_2O_{ICE} \times X_{ICE} + N_2O_{WRW} \times X_{WRW} \quad (10)$$

where X_{ICE} and X_{WRW} represent the proportion of melting ice water and winter residual water in USW, respectively, and S_{ICE} and S_{WRW} represent the salinity of melting ice water and winter residual water, respectively. N_2O_{ICE} and N_2O_{WRW} represent the N_2O concentration of melting ice water and winter residual water, respectively. In this paper, the salinity and N_2O concentration at the bottom of ice cores are used to represent the salinity and N_2O concentration of melting ice water.

3. Results and Discussion

3.1. Structure of Sea Ice

The length of IS05 and IS06 cores were 123 cm and 105 cm, respectively. The top of the cores was 3–5 cm thick with snow, and beneath the snow was columnar ice. For better comparison of the sea ice structure and N_2O distribution in different ice cores, we normalized the length of the two cores (the length of sea ice was processed into a dimensionless number 1, and the sea ice depth becomes a relative value of the total length, $0 < \text{normalized depth} < 1$) [25]. Vertical profiles of temperature, salinity and density against normalized depth are shown in Figure 2, revealing that salinity distribution characteristics of IS05 and IS06 were different. According to the structure and salinity distribution characteristics of sea ice, IS05 is MYI and IS06 is FYI. Since sea ice formed, about 80% of the salt was rejected from sea ice into seawater, and only a small amount of the salt was rejected in the sea ice structure within brine inclusions. As a consequence, the salinity of sea ice was much lower than seawater. This initial desalination is due to gravity drainage throughout all the ice layers [31,32]. The sea ice then enters the second phase in winter; as the temperature and salinity of the lower third sea ice were higher, brine was expelled from ice continuously by gravity drainage, and the bulk salinity decreases by about 3.91‰ throughout the winter. On the contrary, the upper two-thirds of the ice lost contact with the ocean, and the bulk salinity in this portion decreased by only 0.25‰ throughout the winter. Finally, the salinity profile of FYI presented in a C-shape consistent with previous studies [32]. In the summer, sea ice begins the third phase of degeneration. The permeability of the entire core increases due to flushing by the surface melt water, resulting in C-shaped salinity profile of FYI transforming into a typical MYI salinity profile [33–35]. After vigorous desalination in the first year, the desalination of the MYI slows down and reaches an equilibrium by ~10 years because of not enough salinity in sea ice [35]. Generally, the salinity of the upper part of the cores is extremely low due to gravity desalination and flushing by melting ice water, a significant feature that distinguishes the FYI from the MYI.

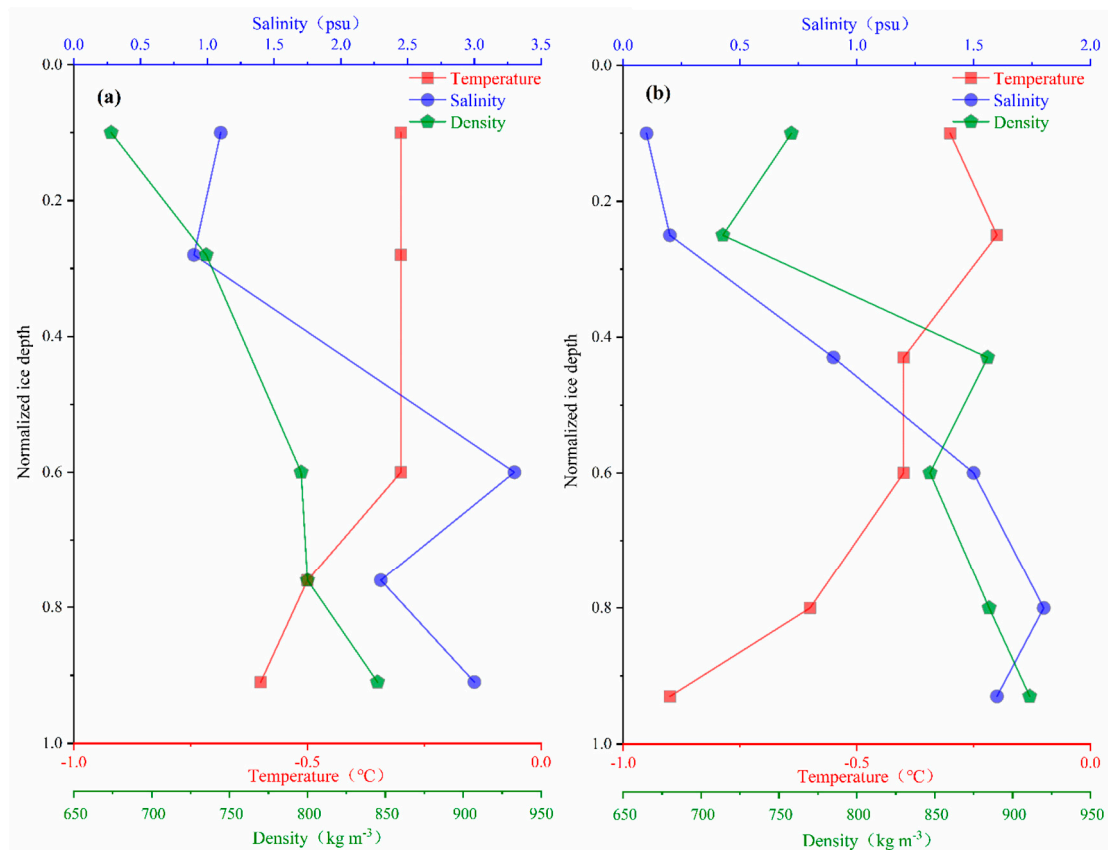


Figure 2. Sea ice salinity, temperature, and density against normalized depth for (a) FYI (20 August 2016) and (b) MYI (18 August 2016) during the melt season.

3.2. Temperature, Salinity, and Density Distributions of Sea Ice

As shown in Figure 2, the temperature range of FYI is from -0.2 to -0.9 °C, and the temperature range of MYI is from -0.3 to -0.6 °C. The sea ice temperature generally presents a distribution characteristic of gradual decline from the surface to the bottom, which is consistent with previous observations [26]. The upper part of the FYI (normalized depth 0~0.6) is an isothermal layer with a temperature close to 0 °C, which is mainly affected by the higher atmospheric temperature. The subsurface (normalized depth 0.2~0.3) temperature of the MYI is slightly higher than that of sea ice due to solar radiation heating the surface and subsurface of sea ice, while the ice surface loses heat by emitting long-wave radiation from its own, resulting in this unique vertical temperature distribution [36,37]. The salinity of FYI ranges from 0.9 to 3.3‰, with an average salinity of 2.1 ± 1.1 . The maximum salinity occurs at the normalized depth of 0.6, while the minimum salinity occurs at the subsurface. The salinity of MYI ranges from 0.1 to 1.8, with an average salinity of 1.0 ± 0.7 . The lowest salinity is similarly located in the subsurface and the highest salinity in a normalized depth of 0.8. As discussed in Section 3.2, the salinity distributions of FYI and MYI were mainly affected by gravity desalination and flushing by melting ice water. The density of FYI ranges from 674 to 875 kg m⁻³, with an average density of 770 ± 66.4 kg m⁻³, and the density of MYI ranges from 714 to 758 kg m⁻³, with an average density of 883 ± 79.2 kg m⁻³. Hence, the density of MYI is higher than FYI. Since the gas volume fraction decreases with the normalized depth, sea ice density shows a similar pattern; the subsurface of MYI is less dense than the surface because it is warmer and melts more heavily.

3.3. Sea Ice Brine and Gas Volume Fractions

The sea ice brine and gas volume fractions are two important basic physical characteristics of sea ice [38]. The distribution of brine and gas in sea ice is difficult to observe in

practice, thus the salinity and volume of brine in sea water are usually calculated according to the empirical formula [39]. Brines encased in ice forms bubbles during phase transition [40]. In parallel to frozen pure water, brine and dissolved gases were rejected from ice crystals, resulting in the accumulation of gas in brine, eventually exceeding saturation and forming bubbles [10,41,42]. Those bubbles and brine, which become part of the sea ice as they were encased, also raise the gas volume fractions of ice. As shown in Figure 3, the gas volume fraction of FYI ranges from 9.7 to 27.6%, with an average of $17.7 \pm 6.8\%$. The gas volume fraction decreases with the increase of normalized depth, whereas the gas volume fraction of MYI ranges from 1.5 to 22.5%, with an average of $10.4 \pm 8.8\%$. The maximum fraction appeared in the subsurface and the lowest fraction appeared near the bottom. The subsurface of MYI rapidly melts due to solar radiation in summer, resulting in the upper part of MYI being air permeable. After the brine is drained, the drained brine pockets are refilled by air [25], resulting in the highest gas volume fraction in the subsurface. Similarly, there are great differences in brine distribution between FYI and MYI: the brine fraction varies from 8.8 to 48.4%, with an average of $23.4 \pm 14.7\%$, and the minimum fraction appears at the subsurface while the maximum fraction appears at the normalized depth of 0.6. The melting process inside the sea ice increases brine volume and reduces brine salinity [43], which change the temperature, salinity and permeability of sea ice, and ultimately affects the brine distribution. The permeability dominates the distribution of gases in sea ice [44]; brine volume fraction greater than 5% means sea ice is permeable for brine [45,46]. Gas migration is more difficult in sea ice, which is hindered by a curved brine network, such that the gas penetration threshold is typically 7–10% [43,47]. It is generally thought that the FYI column is permeable because the brine volume fraction of the whole core is higher than 7%. Similarly, although the brine volume fraction in the MYI surface and subsurface was less than 7%, the brine in these layers have been drained, meaning that the entire MYI column is also permeable to a certain extent. The structural characteristics of sea ice provide a basis for us to discuss the distribution mechanism of N_2O in sea ice.

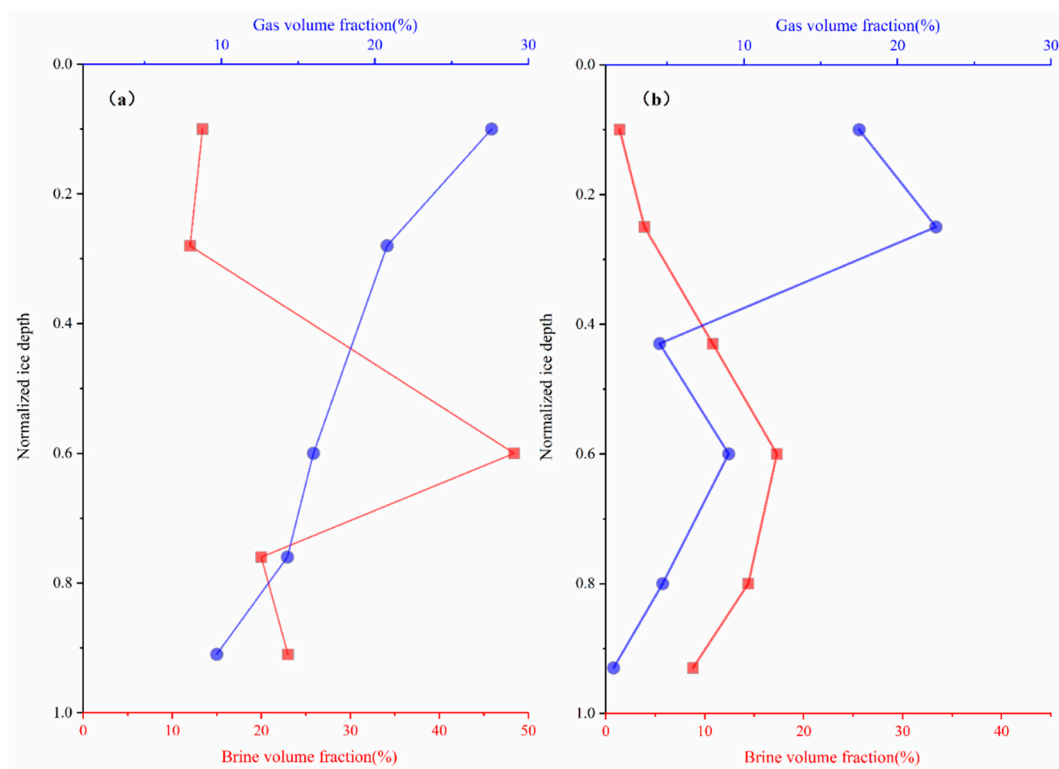


Figure 3. Sea ice brine volume fraction (red points) and gas volume fraction (blue points) versus normalized depth for (a) FYI and (b) MYI.

3.4. N₂O Distribution in Sea Ice

We describe the results of N₂O distribution in sea ice, which are shown in Figure 4. The average N₂O concentration in sea ice was 4.7 ± 1.5 nmol kg⁻¹, slightly lower than 5.2 nmol kg⁻¹ reported by previous studies [48], and the N₂O distribution between FYI and MYI were different from each other. The N₂O concentration of FYI ranged from 3.7 nmol kg⁻¹ to 6.3 nmol kg⁻¹, with an average of 4.5 ± 1.0 nmol kg⁻¹. The lowest concentration occurred in the subsurface layer and the highest was located at the bottom of ice core, whereas the N₂O concentration of MYI ranged from 2.1 nmol kg⁻¹ to 7.7 nmol kg⁻¹, with an average value of 4.8 ± 1.9 nmol kg⁻¹. The lowest concentration was located at the bottom of the sea ice, and the highest occurred in the subsurface of cores. In line with previous studies [48], the average N₂O concentration of MYI was slightly higher than that of FYI, and the N₂O distribution mechanisms of MYI and FYI were dissimilar. The N₂O concentration was higher in the surface ventilated to the atmosphere, and in the bottom in contact with sea water in FYI, while the high N₂O concentration in MYI appeared in the layer with the largest gas volume fractions. It is generally accepted that the N₂O in sea ice mainly exists in two forms: the dissolved phase in brine and the gaseous phase in sea ice gas. The N₂O in the dissolved phase and gaseous phase is transported through the atmosphere-sea ice-seawater system, due to brine dynamics and bubble buoyancy [40].

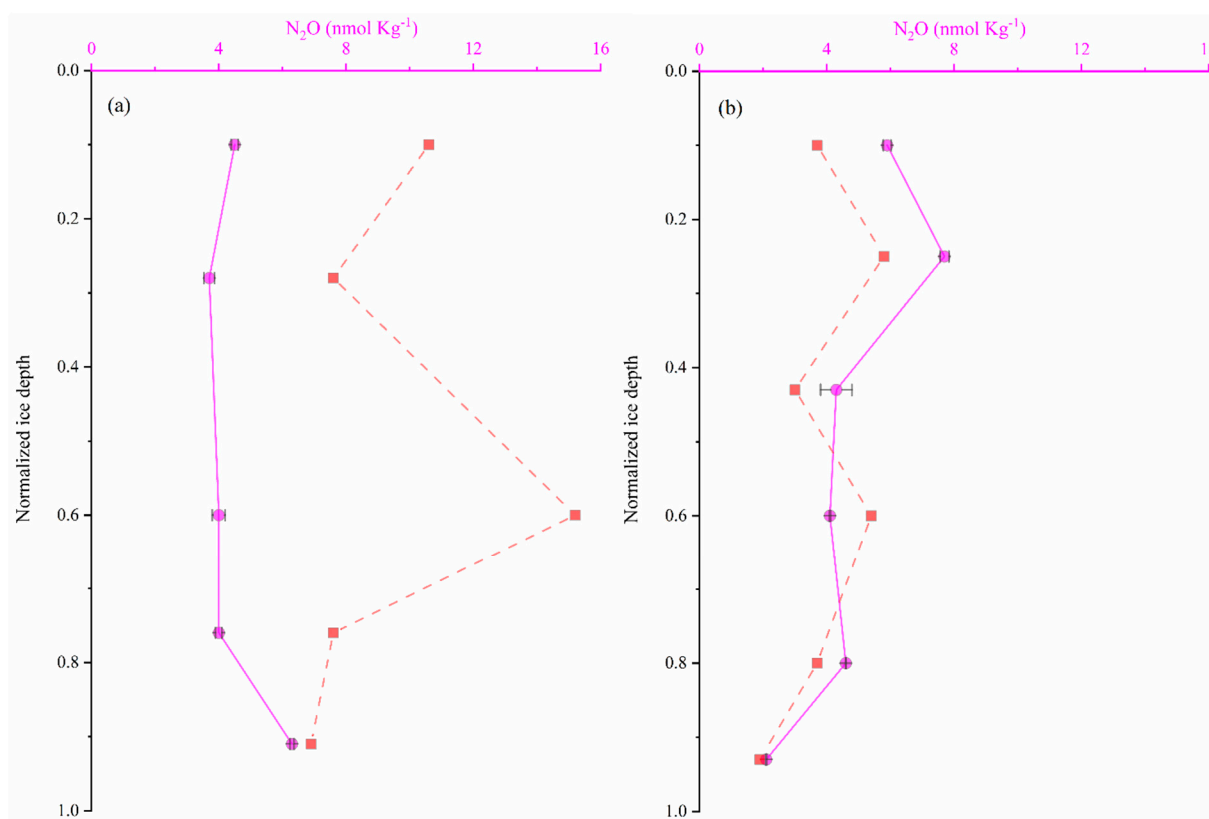


Figure 4. Sea ice observed N₂O (claret line) and T-N₂O_{ice} (red line) concentration versus normalized depth for (a) FYI and (b) MYI.

As shown in Figure 4, we found that the T-N₂O_{ice} of FYI was significantly different from the actual observed N₂O concentration, which was significantly lower than the estimated concentration, and the distribution of N₂O concentration versus normalized depth is also seriously inconsistent. We speculate that this is mainly due to the time period from the start of sea ice melting to our in-situ sampling was too short and led to the incomplete ventilation of FYI. The higher N₂O concentration in the surface was likely caused by the brine expulsion from inside to outside [48], as well as by ventilation at the ice–gas interface [40], while higher N₂O at the bottom of the FYI appears to be influenced

by the exchange at the sea–ice interface or by the possible generation of N_2O under the sea ice. On the contrary, the vertical N_2O distribution versus normalized depth is consistent with that of $T-N_2O_{ice}$, and is positively correlated with the distribution of gas fractions. Atmosphere was allowed to enter the cavity caused by brine expulsion because the MYI was permeable to a certain extent, resulting in the highest N_2O present in the subsurface where the most brine was drained, whereas the low N_2O concentration at the bottom is likely related to the N_2O consumption process at the bottom of cores [49–52], and the bacterial denitrification process at the bottom of sea ice potentially contributes to N_2O consumption [13].

3.5. N_2O Distribution in USW Influenced by Sea Ice Melting Rapidly

Our research on USW (In this study, USW is seawater within a depth of 2 m below sea ice) is shown in Figure 5. The temperature of USW varied from -0.3 °C to -1.2 °C, and the temperature decreased with water depth. Salinity varied from 7.0 to 31.2, and generally increased with water depth. The low-salinity seawater observed in USW indicated that sea ice was melting rapidly in Arctic Ocean. The N_2O concentration varied from 8.7 to 16.7 $nmol\ kg^{-1}$, with an average concentration of 15.0 ± 1.9 $nmol\ kg^{-1}$ and an average saturation of 90.3%, which was in line with previous studies demonstrating that the N_2O concentration at the sea–ice interface was severely unsaturated [48].

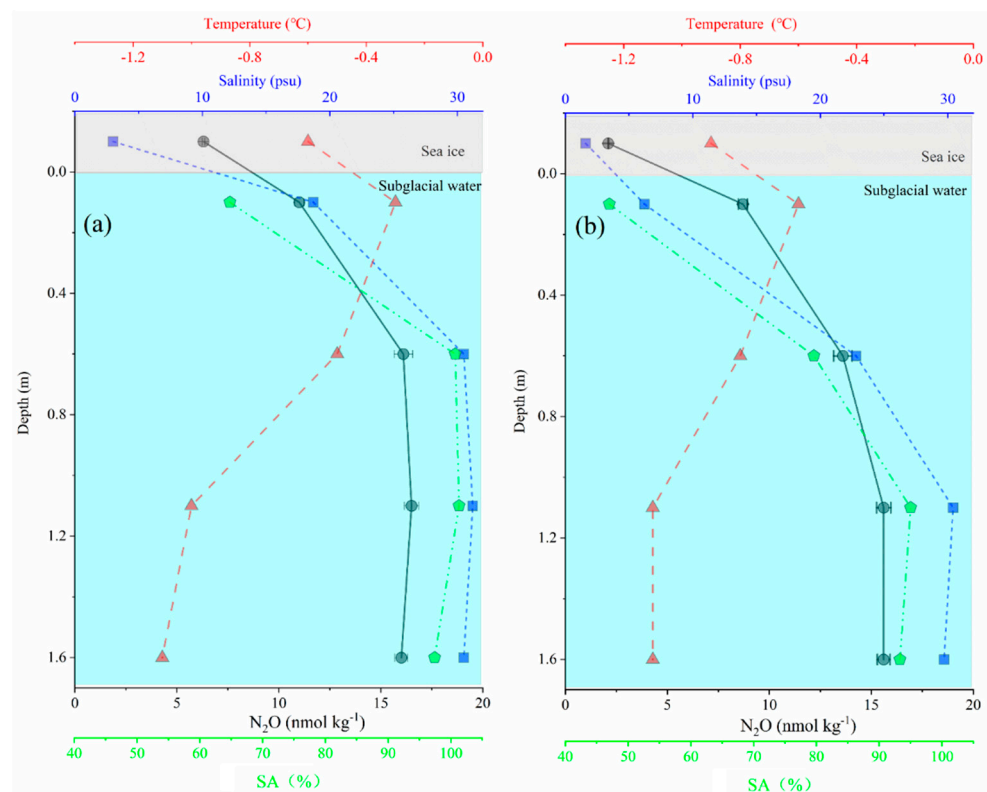


Figure 5. Temperature (red line), salinity (blue line), N_2O concentration (gray line), and N_2O saturation (green line) distribution versus depth in USW for (a) FYI and (b) MYI.

Similar to the vertical distribution of salinity, the distribution of N_2O concentration generally increased with depth. N_2O concentration in USW is generally unsaturated and influenced by meltwater, resulting in USW presenting as a sink of N_2O . The lowest N_2O concentration at the bottom of the MYI corresponds to the lowest N_2O concentration of USW in contact with the sea ice, which also indicates that there is a strong correlation of N_2O distribution between sea ice and USW. The maximum N_2O concentration in USW is 16.7 $nmol\ kg^{-1}$, which is close to the N_2O concentration in the Arctic Ocean winter residual water. The winter residual water is a water mass characterized by a depth of 10–30 m,

temperature less than $-1.3\text{ }^{\circ}\text{C}$, and salinity higher than 32.5 in the Arctic Ocean abyssal basin during CHINARE2016, with an average N_2O concentration of 17.2 nmol kg^{-1} . This water mass retains the characteristics of ‘underlying water’ in winter; consequently, it could serve as the source of seawater for the melting process beneath the sea ice. The melting process of arctic sea ice could be regarded as a mixing process of two end-sources, meltwater and winter residual water. Therefore, we could calculate the respective proportion of the two masses of water in USW after mixing according to the salinity characteristic values of residual water and melting ice water in winter, and then calculate the theoretical N_2O concentration of USW, in which the mixing process is conservative. Taking sea ice meltwater and sea water in USW as end-sources, we calculated the respective proportions of sea ice meltwater and sea water in USW according to salinity, and then calculated the theoretical N_2O ($\text{T-N}_2\text{O}_{\text{USW}}$) concentration of mixed USW. As shown in Figure 6, we found that the observed N_2O concentration was higher than $\text{T-N}_2\text{O}_{\text{USW}}$; the intercept of the trend line describing observed N_2O versus salinity was greater than that describing $\text{T-N}_2\text{O}_{\text{USW}}$ versus salinity. There may be a variety of reasons interpreting this anomaly. For example, it may be caused by the gradient difference of N_2O concentration between USW and subsurface water, resulting in the N_2O in subsurface water being transported to the undersaturated USW along the concentration gradient. Moreover, ventilation that occurs when exposed to the atmosphere also possibly leads to the increase of N_2O concentration in the USW.

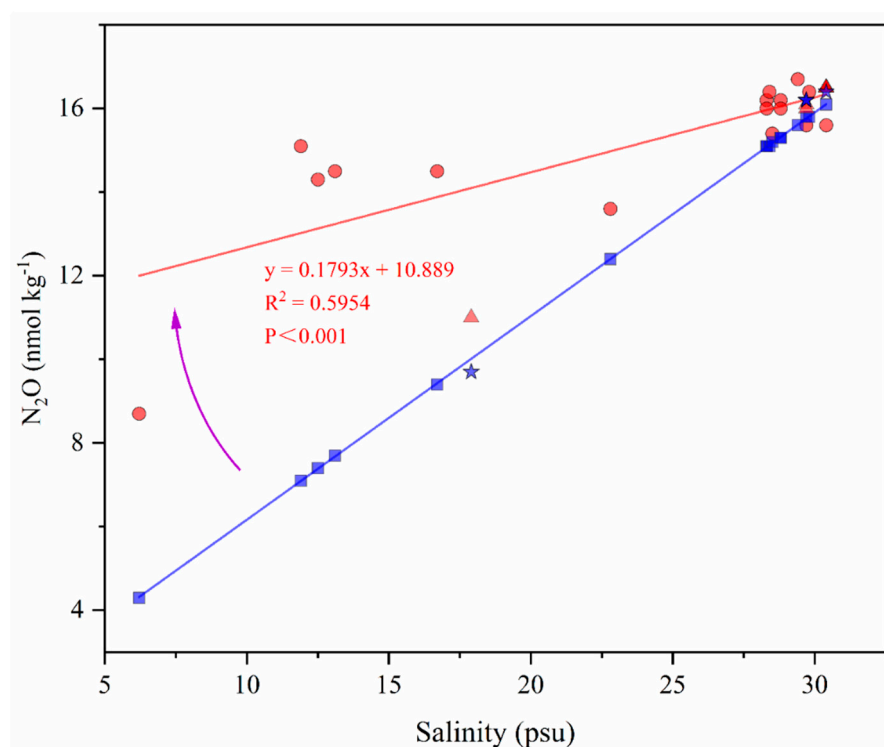


Figure 6. Observed N_2O (red) and $\text{T-N}_2\text{O}_{\text{USW}}$ (blue) concentration versus salinity in USW. The red circles and triangles represent the observed N_2O for MYI and FYI, respectively; the blue rectangles and pentacles represent the $\text{T-N}_2\text{O}_{\text{USW}}$ for MYI and FYI, respectively.

The summer precipitation in the Arctic Ocean ranges from 30 mm mo^{-1} to 60 mm mo^{-1} [53], which causes overestimation of the proportion of meltwater, resulting in a smaller $\text{T-N}_2\text{O}_{\text{USW}}$. However, because of the obstruction of sea ice to the mixing of snowfall and seawater and the lack of water isotope data of water, we could not quantify the impact of precipitation and did not investigate the impact of precipitation in depth. In addition, other studies have shown that there may be a N_2O generation process in the sea ice-seawater system, which may also be one of the reasons why the observed N_2O concentration in glacial water is higher than the theoretical N_2O concentration.

4. Conclusions

The distribution characteristics and driving mechanism of N₂O of sea ice and its USW under rapid melting in Arctic Ocean were studied for the first time in this study. Our results demonstrated that:

(1) There is a significant difference in the N₂O concentration between FYI and MYI; the average N₂O concentration of FYI is $4.5 \pm 1.0 \text{ nmol kg}^{-1}$, ranging from 3.7 to 6.3 nmol kg^{-1} , while MYI is $4.8 \pm 1.9 \text{ nmol kg}^{-1}$, ranging from 2.1 to 7.7 nmol kg^{-1} . The permeability of sea ice is the key factor leading to the differences in N₂O concentration between FYI and MYI, with the interior of FYI being a little ventilated, and the MYI thoroughly ventilated.

(2) The profile in FYI and MYI differs greatly. The N₂O concentration in FYI was high in the surface and bottom of cores and low in the interior of sea ice, while it was low in the bottom layer and high in the subsurface layer in MYI.

(3) The exchange among the atmosphere-sea ice-seawater system, brine desalination, and possible N₂O generation process at the bottom of sea ice are the main driving mechanisms affecting the N₂O distribution of FYI. However, the reasonable amount of ventilation, the gas content of sea ice, and the possible microbial denitrification process at the bottom of sea ice are the main driving mechanisms.

(4) USW is mostly undersaturated with N₂O, with values ranging from 47.2 to 102.2%, owing to the rapid sea ice melting in Arctic Ocean. However, due to the influence of the air-sea exchange, diffusion process, possible N₂O generation mechanism in USW and precipitation, the observed N₂O concentration in glacial water is higher than that of T-N₂O_{USW}. Due to the lack of data at present, a more detailed driving mechanism needs to be further studied and discussed.

The Arctic climate is changing rapidly, resulting in the proportion of FYI and MYI, sea ice structure, and sea ice coverage also changing rapidly, which have an important influence on the N₂O source and sink in the Arctic Ocean. Therefore, it is necessary to further strengthen studies about the effects of sea ice change on N₂O distribution and metabolism in the Arctic Ocean in the future to better evaluate the global N₂O flux in response to global climate change.

Author Contributions: In this manuscript, J.L., L.Z. and L.C. designed the experiments. J.L., J.Z. and Q.W. performed the surveys during CHINARE 2016. Y.L., J.W., W.Y. and M.W. performed experiments in the lab. All authors have read and agreed to the published version of the manuscript.

Funding: This research was funded by the Scientific Research Foundation of Third Institute of Oceanography, MNR (No.2018024, No.2019033), the National Natural Science Foundation of China (No.41676186, No.41506225 and No.41906193), the National Natural Science Foundation of Fujian Province (No.2019J05147).

Institutional Review Board Statement: Not applicable.

Informed Consent Statement: Not applicable.

Data Availability Statement: The data presented in this study are available on request from the corresponding author.

Acknowledgments: Thanks Di Qi for collaborating during CHINARE2016.

Conflicts of Interest: The authors declare that there are no conflict of interest regarding the publication of this article.

References

1. Chen, D.; Rojas, M.; Samset, B.H.; Cobb, K.; Niang, A.D.; Edwards, P.; Emori, S.; Faria, S.H.; Hawkins, E.; Hope, P.; et al. Climate Change 2021: The Physical Science Basis. Contribution of Working Group I to the Sixth Assessment Report of the Intergovernmental Panel on Climate Change. Available online: <https://www.ipcc.ch/> (accessed on 6 September 2021).
2. Tian, H.Q.; Xu, R.T.; Canadell, J.G.; Thompson, R.L.; Winiwarter, W.; Suntharalingam, P.; Davidson, E.A.; Ciais, P.; Jackson, R.B.; Janssens-Maenhout, G.; et al. A comprehensive quantification of global nitrous oxide sources and sinks. *Nature* **2020**, *586*, 248–256. [[CrossRef](#)]

3. Harada, N. Review: Potential catastrophic reduction of sea ice in the western Arctic Ocean: Its impact on biogeochemical cycles and marine ecosystems. *Glob. Planet. Chang.* **2016**, *136*, 1–17. [[CrossRef](#)]
4. Vihma, T. Effects of arctic sea ice decline on weather and climate: A review. *Surv. Geophys.* **2014**, *35*, 1175–1214. [[CrossRef](#)]
5. Meier, W.N.; Hovelsrud, G.K.; van Oort, B.E.H.; Key, J.R.; Kovacs, K.M.; Michel, C.; Haas, C.; Granskog, M.A.; Gerland, S.; Perovich, D.K.; et al. Arctic sea ice in transformation: A review of recent observed changes and impacts on biology and human activity. *Rev. Geophys.* **2014**, *52*, 185–217. [[CrossRef](#)]
6. Zhan, L.Y.; Zhang, J.X.; Ouyang, Z.X.; Lei, R.B.; Xu, S.Q.; Qi, D.; Gao, Z.Y.; Sun, H.; Li, Y.H.; Wu, M.; et al. High-resolution distribution pattern of surface water nitrous oxide along a cruise track from the Okhotsk Sea to the western Arctic Ocean. *Limnol. Oceanogr.* **2020**, *66*, S401–S410. [[CrossRef](#)]
7. Zhang, J.X.; Zhan, L.Y.; Chen, L.Q.; Li, Y.H.; Chen, J.F. Coexistence of nitrous oxide undersaturation and oversaturation in the surface and subsurface of the western Arctic Ocean. *J. Geophys. Res.-Ocean.* **2015**, *120*, 8392–8401. [[CrossRef](#)]
8. Toyoda, S.; Kakimoto, T.; Kudo, K.; Yoshida, N.; Sasano, D.; Kosugi, N.; Ishii, M.; Kameyama, S.; Inagawa, M.; Yoshikawa-Inoue, H.; et al. Distribution and production mechanisms of N₂O in the western Arctic Ocean. *Glob. Biogeochem. Cycles* **2021**, *35*, e2020GB006881. [[CrossRef](#)]
9. Comiso, J.C.; Parkinson, C.L.; Gersten, R.; Stock, L. Accelerated decline in the Arctic Sea ice cover. *Geophys. Res. Lett.* **2008**, *35*, L01703. [[CrossRef](#)]
10. Loose, B.; McGillis, W.R.; Schlosser, P.; Perovich, D.; Takahashi, T. Effects of freezing, growth, and ice cover on gas transport processes in laboratory seawater experiments. *Geophys. Res. Lett.* **2009**, *36*, L05603. [[CrossRef](#)]
11. Delille, B.; Jourdain, B.; Borges, A.V.; Tison, J.L.; Delille, D. Biogas (CO₂, O₂, dimethylsulfide) dynamics in spring Antarctic fast ice. *Limnol. Oceanogr.* **2007**, *52*, 1367–1379. [[CrossRef](#)]
12. Rysgaard, S.; Bendtsen, J.; Pedersen, L.T.; Ramlov, H.; Glud, R.N. Increased CO₂ uptake due to sea ice growth and decay in the Nordic Seas. *J. Geophys. Res.-Ocean.* **2009**, *114*, C09011. [[CrossRef](#)]
13. Randall, K.; Scarratt, M.; Lefebvre, M.; Michaud, S.; Xie, H.X.; Gosselin, M. First measurements of nitrous oxide in Arctic sea ice. *J. Geophys. Res.-Ocean.* **2012**, *117*, 8. [[CrossRef](#)]
14. Anderson, L.G.; Falck, E.; Jones, E.P.; Jutterstrom, S.; Swift, J.H. Enhanced uptake of atmospheric CO₂ during freezing of seawater: A field study in Storfjorden, Svalbard. *J. Geophys. Res.-Ocean.* **2004**, *109*, C06004. [[CrossRef](#)]
15. Kitidis, V.; Upstill-Goddard, R.C.; Anderson, L.G. Methane and nitrous oxide in surface water along the north-west passage, Arctic Ocean. *Mar. Chem.* **2010**, *121*, 80–86. [[CrossRef](#)]
16. Yamamoto-Kawai, M.; McLaughlin, F.A.; Carmack, E.C.; Nishino, S.; Shimada, K. Aragonite undersaturation in the Arctic Ocean: Effects of ocean acidification and sea ice melt. *Science* **2009**, *326*, 1098–1100. [[CrossRef](#)]
17. Thompson, D.W.J.; Wallace, J.M. The Arctic Oscillation signature in the wintertime geopotential height and temperature fields. *Geophys. Res. Lett.* **1998**, *25*, 1297–1300. [[CrossRef](#)]
18. Proshutinsky, A.Y.; Johnson, M.A. Two circulation regimes of the wind driven Arctic Ocean. *J. Geophys. Res.-Ocean.* **1997**, *102*, 12493–12514. [[CrossRef](#)]
19. Proshutinsky, A.Y.; Polyakov, I.V.; Johnson, M.A. Climate states and variability of Arctic ice and water dynamics during 1946–1997. *Polar Res.* **1999**, *18*, 135–142. [[CrossRef](#)]
20. Dickson, B. Oceanography—All change in the Arctic. *Nature* **1999**, *397*, 389–391. [[CrossRef](#)]
21. Serreze, M.C.; Holland, M.M.; Stroeve, J. Perspectives on the Arctic’s shrinking sea-ice cover. *Science* **2007**, *315*, 1533–1536. [[CrossRef](#)]
22. Binder, H.; Boettcher, M.; Grams, C.M.; Joos, H.; Pfahl, S.; Wernli, H. Exceptional air mass transport and dynamical drivers of an extreme wintertime arctic warm event. *Geophys. Res. Lett.* **2017**, *44*, 12028–12036. [[CrossRef](#)]
23. Stroeve, J.; Holland, M.M.; Meier, W.; Scambos, T.; Serreze, M. Arctic sea ice decline: Faster than forecast. *Geophys. Res. Lett.* **2007**, *34*, L09501. [[CrossRef](#)]
24. Liu, J.P.; Song, M.R.; Horton, R.M.; Hu, Y.Y. Reducing spread in climate model projections of a September ice-free Arctic. *Proc. Natl. Acad. Sci. USA* **2013**, *110*, 12571–12576. [[CrossRef](#)]
25. Wang, Q.; Lu, P.; Lepparanta, M.; Cheng, B.; Zhang, G.; Li, Z. Physical properties of summer sea ice in the pacific sector of the arctic during 2008–2018. *J. Geophys. Res.-Ocean.* **2020**, *125*, e2020JC016371. [[CrossRef](#)]
26. Carnat, G.; Papakyriakou, T.; Geilfus, N.X.; Brabant, F.; Delille, B.; Vancoppenolle, M.; Gilson, G.; Zhou, J.Y.; Tison, J.L. Investigations on physical and textural properties of Arctic first-year sea ice in the Amundsen Gulf, Canada, November 2007–June 2008 (IPY-CFL system study). *J. Glaciol.* **2013**, *59*, 819–837. [[CrossRef](#)]
27. Eicken, H.; Bluhm, B.A.; Collins, R.E.; Haas, C.; Ingham, M.; Gradinger, R.; Mahoney, A.; Nicolaus, M.; Perovich, D.K. *Field Cold Regions Science and Marine Technology, Encyclopedia of Life Support Systems (EOLSS); Techniques in Sea-Ice Research; UNESCO, EOLSS Publishers: Prais, France, 2014.*
28. Zhan, L.-Y.; Chen, L.-Q.; Zhang, J.-X.; Lin, Q. A system for the automated static headspace analysis of dissolved N₂O in seawater. *Int. J. Environ. Anal. Chem.* **2013**, *93*, 828–842. [[CrossRef](#)]
29. Weiss, R.F.; Price, B.A. Nitrous oxide solubility in water and seawater. *Mar. Chem.* **1980**, *8*, 347–359. [[CrossRef](#)]
30. Leppäranta, M.; Manninen, T. *The Brine and Gas Content of Sea Ice with Attention to Low Salinities and High Temperatures; Finnish Institute of Marine Research: Helsinki, Finland, 1988.*

31. Worster, M.G.; Wettlaufer, J.S. Natural convection, solute trapping, and channel formation during solidification of saltwater. *J. Phys. Chem. B* **1997**, *101*, 6132–6136. [[CrossRef](#)]
32. Nakawo, M.; Sinha, N.K. Growth-rate and salinity profile of 1st-year sea ice in the high arctic. *J. Glaciol.* **1981**, *27*, 315–330. [[CrossRef](#)]
33. Tucker, W.B.; Gow, A.J.; Weeks, W.F. Physical-properties of summer sea ice in the fram strait. *J. Geophys. Res.-Ocean.* **1987**, *92*, 6787–6803. [[CrossRef](#)]
34. Cottier, F.; Eicken, H.; Wadhams, P. Linkages between salinity and brine channel distribution in young sea ice. *J. Geophys. Res.-Ocean.* **1999**, *104*, 15859–15871. [[CrossRef](#)]
35. Vancoppenolle, M.; Fichet, T.; Bitz, C.M. Modeling the salinity profile of undeformed Arctic sea ice. *Geophys. Res. Lett.* **2006**, *33*, 5. [[CrossRef](#)]
36. Overgaard, S.; Wadhams, P.; Lepparanta, M. Ice properties in the Greenland and Barents seas during summer. *J. Glaciol.* **1983**, *29*, 142–164. [[CrossRef](#)]
37. Cheng, B.; Zhang, Z.H.; Vihma, T.; Johansson, M.; Bian, L.G.; Li, Z.J.; Wu, H.D. Model experiments on snow and ice thermodynamics in the Arctic Ocean with CHINARE 2003 data. *J. Geophys. Res.-Ocean.* **2008**, *113*, C09020. [[CrossRef](#)]
38. Light, B.; Maykut, G.A.; Grenfell, T.C. A temperature-dependent, structural-optical model of first-year sea ice. *J. Geophys. Res.-Ocean.* **2004**, *109*, C06013. [[CrossRef](#)]
39. Cox, G.F.N.; Weeks, W.F. Equations for determining the gas and brine volumes in sea-ice samples. *J. Glaciol.* **1983**, *29*, 306–316. [[CrossRef](#)]
40. Crabeck, O.; Galley, R.; Delille, B.; Else, B.; Geilfus, N.X.; Lemes, M.; Des Roches, M.; Francus, P.; Tison, J.L.; Rysgaard, S. Imaging air volume fraction in sea ice using non-destructive X-ray tomography. *Cryosphere* **2016**, *10*, 1125–1145. [[CrossRef](#)]
41. Killawee, J.A.; Fairchild, I.J.; Tison, J.L.; Janssens, L.; Lorrain, R. Segregation of solutes and gases in experimental freezing of dilute solutions: Implications for natural glacial systems. *Geochim. Cosmochim. Acta* **1998**, *62*, 3637–3655. [[CrossRef](#)]
42. Tison, J.L.; Haas, C.; Gowing, M.M.; Sleewaegen, S.; Bernard, A. Tank study of physico-chemical controls on gas content and composition during growth of young sea ice. *J. Glaciol.* **2002**, *48*, 177–191. [[CrossRef](#)]
43. Zhou, J.Y.; Delille, B.; Eicken, H.; Vancoppenolle, M.; Brabant, F.; Carnat, G.; Geilfus, N.X.; Papakyriakou, T.; Heinesch, B.; Tison, J.L. Physical and biogeochemical properties in landfast sea ice (Barrow, Alaska): Insights on brine and gas dynamics across seasons. *J. Geophys. Res.-Ocean.* **2013**, *118*, 3172–3189. [[CrossRef](#)]
44. Eicken, H.; Krouse, H.R.; Kadko, D.; Perovich, D.K. Tracer studies of pathways and rates of meltwater transport through Arctic summer sea ice. *J. Geophys. Res.-Ocean.* **2002**, *107*, SHE 22-1–SHE 22-20. [[CrossRef](#)]
45. Golden, K.M.; Eicken, H.; Heaton, A.L.; Miner, J.; Pringle, D.J.; Zhu, J. Thermal evolution of permeability and microstructure in sea ice. *Geophys. Res. Lett.* **2007**, *34*, L16501. [[CrossRef](#)]
46. Golden, K.M.; Ackley, S.F.; Lytle, V.I. The percolation phase transition in sea ice. *Science* **1998**, *282*, 2238–2241. [[CrossRef](#)] [[PubMed](#)]
47. Moreau, S.; Vancoppenolle, M.; Zhou, J.Y.; Tison, J.L.; Delille, B.; Goosse, H. Modelling argon dynamics in first-year sea ice. *Ocean Model. Online* **2014**, *73*, 1–18. [[CrossRef](#)]
48. Marie, K. *CO₂ and N₂O Dynamics in the Ocean–Sea Ice–Atmosphere System*; Université de Liège: Liège, Belgium, 2019.
49. Rysgaard, S.; Glud, R.N. Anaerobic N₂ production in Arctic sea ice. *Limnol. Oceanogr.* **2004**, *49*, 86–94. [[CrossRef](#)]
50. Rysgaard, S.; Glud, R.N.; Sejr, M.K.; Blicher, M.E.; Stahl, H.J. Denitrification activity and oxygen dynamics in Arctic sea ice. *Polar Biol.* **2008**, *31*, 527–537. [[CrossRef](#)]
51. Nomura, D.; Yoshikawa-Inoue, H.; Toyota, T. The effect of sea-ice growth on air-sea CO₂ flux in a tank experiment. *Tellus Ser. B-Chem. Phys. Meteorol.* **2006**, *58*, 418–426. [[CrossRef](#)]
52. Kaartokallio, H. Evidence for active microbial nitrogen transformations in sea ice (Gulf of Bothnia, Baltic Sea) in midwinter. *Polar Biol.* **2001**, *24*, 21–28. [[CrossRef](#)]
53. Boisvert, L.N.; Webster, M.A.; Petty, A.A.; Markus, T.; Bromwich, D.H.; Cullather, R.I. Intercomparison of precipitation estimates over the arctic ocean and its peripheral seas from reanalyses. *J. Clim.* **2018**, *31*, 8441–8462. [[CrossRef](#)]